Please provide feedback

Please support the ScholarWorks@UMBC repository by emailing scholarworks-group@umbc.edu and telling us what having access to this work means to you and why it's important to you. Thank you.

1   **Ocean stratification and sea-ice cover in Barents and Kara seas modulate sea-air**

2   **methane flux: satellite evidence**

3   **L. Yurganov[1], D. Carroll[2] , and H. Zhang[3]**

4   [1]University of Maryland Baltimore County, Baltimore, Maryland, USA

5   [2] .Moss Landing Marine Laboratories, San José State University, CA, USA

6   [3]Jet Propulsion Laboratory, California Institute of Technology, CA, USA

7   Corresponding author: Leonid Yurganov (Leonid.Yurganov@gmail.com)

8   **Key Points:**

9   • Positive methane anomalies over the Barents and Kara Seas in winter coincide with
10   increasing mixed layer depth.

11   • Seventeen years of satellite AIRS data reveal areas of enhanced rates of methane growth
12   in the northern Barents/Kara Arctic region.

13   • The methane seasonal cycle amplitude grows from 2002 to 2019 most rapidly over areas
14   with maximal rates of sea-ice degradation.

15

16   **INDEX TERMS**

17   **0312 Air/sea constituent fluxes**

18   **1615 Biogeochemical cycles, processes, and modeling**

19   **1640 Remote sensing**

20   **3002 Continental shelf and slope processes**

21   **3004   Gas   and   hydrate   systems**

22 **Abstract**

23 The diverse range of mechanisms driving the Arctic amplification are not completely understood
24 and, moreover, the role of the greenhouse gas methane in Arctic warming remains unclear.
25 Strong sources of methane at the ocean seabed in the Barents Sea and other polar regions are
26 well documented. Nevertheless, those data suggest that negligible amounts of methane fluxed
27 from the seabed enter the atmosphere, with roughly 90% of the methane consumed by bacteria.
28 The observations are taken during summer, which is favorable for collecting data but also
29 characterized by a strongly-stratified water column. In winter the stratification weakens and after
30 a breakdown of the pycnocline, convection, storms, and turbulent diffusion can mix the full-
31 depth water column in high latitudes. The Mixed Layer Depth (MLD) in the ice-free
32 Central/Southern Barents Sea is deepening and the ocean-atmosphere methane exchange
33 increases. An additional barrier for the air-sea flux is seasonally and interannually variable sea-
34 ice cover in partially ice-covered seas. We present Thermal IR space-based spectrometer data
35 between 2002 and 2019 that shows increased methane concentration anomalies over the Barents
36 and Kara seas in winter months. The seasonal methane cycle amplitude north of the Kara Sea has
37 more than doubled since the beginning of the century; this may be interpreted as an effect of sea-
38 ice decline and/or an evidence for growth of seabed emissions. A progressing degradation of
39 Arctic sea-ice cover may lead to increased methane flux and, through a positive feedback loop,
40 to further warming.

41 **Plain Language Summary**

42 Long-term satellite measurements of methane over the Arctic Ocean evidence that vertical
43 seawater mixing is a significant factor that affects its concentration in the troposphere in winter.
44 The methane seasonal amplitude over the northern Kara Sea has increased since the beginning of
45 this century and a decline of the sea ice may be a reason for that.

46 **1 Introduction**

47   The Arctic has experienced the fastest warming on Earth over recent decades, with the
48 Arctic Ocean warming at nearly double the rate of the global ocean (Hoegh-Guldberg and Bruno,
49 2010). The area, thickness, and concentration of sea-ice cover, has been significantly reduced
50 (Comiso et al., 2008; Årthun et al., 2019). There is concern about the release of large amounts of
51 the climate-active greenhouse gas methane (CH_4) from hydrates, permafrost, and other seabed
52 reservoirs (James et al., 2016). The radiation warming potential of methane is 28–34 times that
53 of carbon dioxide (CO_2) over a 100-year period (Myhre et al., 2013). The Barents and Kara seas
54 (BKS) have extensive reserves of oil and natural gas (Shipilov and Murzin, 2002). Thermogenic
55 (fossil) methane seeps through faults in sedimentary layers in the BKS. For example, Serov et al.
56 (2017) reported on intensive cold seep activity clustered on the tops of several ~500-m-wide
57 domes at depths of 370–390 m in Storfjordrenna, northwestern Barents Sea. A review article
58 (James et al., 2016) describes the principal processes that regulate methane distribution in Arctic
59 seafloor sediments, modification in the water column, and subsequent release to the atmosphere.
60 Enhanced concentrations of dissolved methane in the Arctic Ocean seawater are widely
61 observed; these are related, in part, to direct seeps of thermogenic methane, dissociation of gas
62 hydrates and thawing of submerged permafrost. Methane is slowly oxidized by methanotrophic
63 bacteria in oceanic deep layers below the pycnocline with timescales of weeks or years (James et
64 al., 2016). As noted by James et al. (2016), the effect of reduced sea-ice cover on ocean-to-
65 atmosphere methane emissions are especially poorly constrained. The satellite data presented
66 here allow one to fill this critical gap. Warm Atlantic currents make the BKS a climatically
67 important region (Skagseth et al. , 2020). A decline in BKS sea-ice in early winter influences

68 synoptic processes across the northern hemisphere (Petoukhov and Semenov, 2010; Årthun et al.,
69 2019). The Barents Sea is a shallow sea (average depth 230 m), with depressions up to 400 m.
70 The Kara Sea is even shallower (average depth 100 m). The release of methane from the seabed
71 as a result of degradation of the submarine permafrost (Portnov et al., 2014) is expected in the
72 Kara and southern Barents Seas. The most of Barents Sea is free of sea-ice year-round, while
73 winter sea-ice cover in the Kara Sea, as well as in the northernmost Barents Sea, underwent a
74 dramatic decline since early 2000s (Zhang et al., 2018b).

75   The presence of sources is just one necessary condition for methane to enter the
76 atmosphere; transport of the gas from the seafloor to the ocean surface is also critically
77 important. According to Rudels (1993), the relatively warm and salty layer of Atlantic Water
78 (AW) provides a stratified barrier that can inhibit the penetration of dissolved gases into the
79 ocean-surface layer during summer/early autumn (between June and October). Numerous direct
80 studies have shown that during this season the flux in the Barents-Svalbard area is negligible
81 (Gentz et al., 2014; Myhre et al., 2016; Mau et al., 2017). These field investigations, however,
82 also identified strong sources at the seafloor and large concentrations of dissolved methane in
83 deep ocean waters. Therefore, the flux of methane may be significant only after a breakdown of
84 the pycnocline in November, and subsequent deepening of the MLD. The MLD increases sharply
85 in November, with the bulk of the Barents Sea water column mixed by December (Kara et al.,
86 2002). Increased turbulent diffusion is expected to facilitate methane fluxes to the atmosphere.

87   Methane over the BKS was measured from space by IASI (Infrared Atmospheric
88 Sounding Interferometer) and AIRS (Atmospheric InfraRed Sounder) sounders (Yurganov et al,
89 2016, 2017, and 2019). Preliminarily, Yurganov et al. (2016) assessed the annual Arctic Ocean
90 CH_4 emissions in 2010-2014 as ~ 2/3 of land CH_4 emission for north of 60° N. Saunois et al.
91 (2020) estimated the latter as 23 ± 1 Tg CH_4 per year. So, the Arctic marine emission may be as
92 large as 15 Tg CH_4 per year. Satellite observations in the Thermal IR (TIR) range are extremely
93 useful for characterizing methane over ocean regions, particularly during the polar night. Other
94 observational approaches, such as space-borne Short-Wave IR sensors (e.g., TROPOMI, the
95 TROPOspheric Monitoring Instrument) require sunlight and cannot make observations during
96 the polar night (Supplement Figure S1). Additionally, ship-based observations are logistically
97 challenging in these ice-choked regions. Here we analyze methane concentrations in the lowest
98 tropospheric layer over BKS estimated from AIRS/Aqua, IASI-1/MetOp-A with a focus on the
99 November–January period. Data from the Cross-Track Infrared Sounder (CrIS) deployed at the
100 Suomi National Polar-orbiting Partnership (SNPP) platform for 2015–2019 (Bloom, 2001)) were
101 used as well. These data are coupled with regular satellite microwave measurements of sea-ice
102 concentration, described by Cavalieri et al. (1996). MLD was computed from the "Estimating the
103 Circulation and Climate of the Ocean" (ECCO) consortium (Wunsch et al., 2009) ocean state
104 estimate. We find that both vertical mixing and sea-ice cover significantly impacted methane
105 concentrations. Our results provide a basis for predicting the growth of future Arctic Ocean
106 methane emissions, in assumption that sea-ice cover continues to decline.

107 **2 Methods**

108 2.1 Satellite instruments, methane data, and retrieval techniques

109   AIRS, IASI, anf CrIS belong to the TIR group of hyper-spectral sounders (their
110 characteristics are listed by Smith and Barnet (2019)). An important advantage of them is a
111 capability to work at night and over water surface. A disadvantage is a reduced sensitivity to
112 lower troposphere (Yurganov et al., 2016).

113   The AIRS diffraction grating spectrometer was launched in a sun-synchronous polar orbit

114   in May 2002 on board the Aqua satellite (Xiong et al., 2008). The instrument scans ± 48.3°
115   from the nadir, which provides full daily coverage in the Arctic. Spectral resolution is 1.5 cm^{-1} at
116   the methane ν4 absorption band near 7.65 μm. Currently (August 2020), the AIRS is still
117   operational. Starting in September 2002, methane data were processed consistently using
118   version 6 of the standard algorithm developed by NASA (Susskind et al., 2014). Monthly
119   average Level 3 methane, surface and air temperatures between October 2002 and January 2020,
120   both ascending and descending orbits, are available on-line on a 1°x1° latitude/longitude grid
121   (AIRS3STM.006): https://disc.gsfc.nasa.gov/datasets/. Methane profiles were obtained for a 3×3
122   matrix of 9 pixels with a diameter of 13.5 km in nadir each.

123   The IASI-1/MetOp-A is a cross-track-scanning Michelson interferometer that measures
124   spectra of outgoing long wave radiation with an apodized resolution of 0.5 cm−1 in the TIR
125   spectral range that includes the ν4 CH_4 band near 7.65 μm wavelength (Razavi et al., 2009). The
126   MetOp-A satellite, operated by EUMETSAT, was launched in 2006. Like AIRS, IASI has a
127   2200-km swath with a scan swath angle of ±48.3°. The IASI retrieval algorithm NUCAPS was
128   built at NOAA/NESDIS to emulate the AIRS Version 5 code and has been in operation since
129   2008 (Maddy et al., 2009; Gambacorta, 2013). Level 2 data for 2×2 matrices of 4 circular, 12-km
130   diameter   pixels   are   available   from   the   NOAA's   CLASS   site
131   https://www.avl.class.noaa.gov/saa/products/search?sub_id=0&datatype_family=IASI&submit.x=27&submit.y=10.

132   The CrIS is a Michelson interferometer deployed at the SuomiNPP platform launched in
133   October, 2011, in a sun-synchronous polar orbit. Apodized full spectral resolution is 0.75 cm^{-1}.
134   Methane profiles were obtained for a 3×3 matrix of 9 pixels with a diameter of 14 km in nadir
135   each. Retrieval technique CLIMCAPS was developed in Science and Technology Corporation,
136   Columbia, MD, and funded by NASA (Smith and Barnet, 2019). The Level 2 data coded as
137   SNDRSNIML2CCPRET are available from the Goddard Earth Sciences Data and Information
138   Services Center (GES DISC), https://disc.gsfc.nasa.gov/datasets/SNDRSNIML2CCPCCR_2/summary.

139   The Thermal IR reliable measurements require the surface to be warmer than air above it.
140   The data were filtered for cases of Thermal Contrast ThC> 10° C (Yurganov et al., 2016 and
141   Supplement Figures S2 and S3) , where ThC = T_{surf}-T_{600} , T_{surf} is surface temperature, and T_{600}
142   is air temperature at 600 hPa air pressure . Figure S4 in the Supplement illustrates influence of
143   filtering for AIRS data.

144   The profiles were averaged for the lower troposphere (LT) from the surface to the level of
145   600 hPa (~ 4 km) and from 600 hPa to 400 hPa (mid troposphere, MT). The sensitivity to
146   methane variations in the LT and MT was estimated empirically by comparison with
147   simultaneous aircraft measurements at three stations in the United States (Yurganov et al., 2019,
148   and Supplement Figure S4). LT sensitivity was found in the range of 0.3-0.5. MT sensitivity was
149   estimated as 0.8-1.2, i.e., significantly higher. A physical meaning of the empirical sensitivity is
150   a change in retrieved concentration that corresponds to the unit change of the "true" value. E.g.,
151   the sensitivity 0.5 means that real variations (not concentrations themselves) are underestimated
152   by 100%. For the first glance, preference should be made to mid tropospheric data. However,
153   variations of mid tropospheric data are critically dependent on air transport. So, we have chosen
154   to focus on the LT data in attempt to get information on methane as close as possible to the
155   surface. Data for MT are placed in the Supplement (Figures S5, S6, and S7).

156   2.2 ECCO Estimates of Mixed Layer Depth

157   To compute MLD, we use the ECCO LLC270 global ocean and sea-ice data synthesis
158   (Zhang et al., 2018a). ECCO LLC270 is built upon two previous ECCO efforts, ECCO v4
159   (Forget et al., 2015) and ECCO2 (Menemenlis et al., 2005a, 2005b, 2008; Fenty et al., 2017).
160   Compared to the lower-resolution ECCO v4 synthesis (nominal 1° grid spacing), ECCO LLC270

161   has finer horizontal grid spacing (~1/3° at the equator and ~18 km at high latitudes). The vertical
162   discretization comprises 50 z-levels; model integration spans January 1992 to December 2018.
163   Terrestrial runoff along coastal boundaries is forced using the monthly climatology of Fekete et
164   al. (2002). Since horizontal resolution is insufficient to resolve mesoscale eddies, their impact on
165   the large-scale ocean circulation is parameterized using the Redi (1982) and Gent and
166   McWilliams (1990) schemes.

167   We compute monthly-mean LLC 270 MLD using three criteria: (1) when the potential
168   density is greater than surface-ocean density x 0.125 kg m^{-3} (Suga et al., 2004); (2) when the
169   potential density is larger than surface-ocean density ρ by 0.8°C x α, where ρ is the density and α
170   is the seawater thermal expansion coefficient at the ocean surface (Kara et al., 2000); and (3)
171   when the potential density is greater than surface-ocean density + 0.03 kg m^{-3} (Boyer et al.,
172   2004). Kara et al. (2002) compared calculations by criterion #2 with field measurements and
173   confirmed that method accuracy is better than 20 m.

174   2.3 Satellite Sea-ice Observations

175   Sea-ice concentration data are archived by the NASA National Snow and Ice Data Center
176   Distributed Active Archive Center (https://nsidc.org/data/NSIDC-0081/versions/1; described by
177   Cavalieri et al., 1996). The mean monthly data set for November, 2003–January, 2020 is
178   generated from the surface brightness temperature data and is designed to provide a consistent
179   time series of sea-ice concentration C_{ice} (the fraction of ice for each 20×20 km^2 pixel) spanning
180   the coverage of two passive microwave instruments developed as a part of the Defense
181   Meteorological Satellite Program (DMSP), DMSP-F8 and Special Sensor Microwave
182   Imager/Sounder (SSMIS) DMSP-F17. In this paper, we use also the fraction of open water: C_{wat}
183   $= 1 – C_{ice}$ for comparison with concentration and seasonal cycles of methane.

184   **3 Results**

185   Maps of monthly mean LT Arctic methane concentrations for 2013, retrieved from the
186   IASI-1 orbital measurements, have been published by Yurganov et al., (2016) and for 2018 by
187   Yurganov et al. (2019). Here we present seasonal maps for the period between February, 2019
188   and January, 2020, retrieved from AIRS data. All data were binned into 3-month seasons,
189   conditionally named "spring" (Feb–Apr.), "summer" (May–Jul), "autumn" (Aug–Oct.), and
190   "winter" (Nov–Jan) (Figure 1). The summer methane distribution over the Arctic (Figure 1b) is
191   essentially flat, but in autumn–winter (Figure 1c and 1d) peculiar positive anomalies were
192   observed over BKS and other seas. Similar anomalies. but less contrast, were observed for MT
193   altitudes between 4 and 6 km (Supplement, Figure S5). To study this phenomenon, three domains
194   were selected (Figure 1). Domain #1 is free of sea-ice in winter, and is located in the relatively
195   deep western Barents Sea (mean depth 379 m). Domain # 2 is located between three
196   archipelagos: Franz-Joseph Land (FJL), Severnaya Zemlya (SZ) and Novaya Zemplya (NZ). It is
197   shallower (mean depth 82 m) and partially covered by sea-ice. A control domain #3 with mean
198   depth 2053 m was selected in the Norwegian Sea.

199   Monthly mean concentrations for domains # 1 and # 3, retrieved from data of three space-
200   borne spectrometers covering 2010–2018, were computed. Figure 2 shows the general agreement
201   between excess methane in domain #1 (differences between domains 1 and 3) delivered by three
202   independently operating instruments: IASI, AIRS, and CrIS. All three demonstrate a maximum
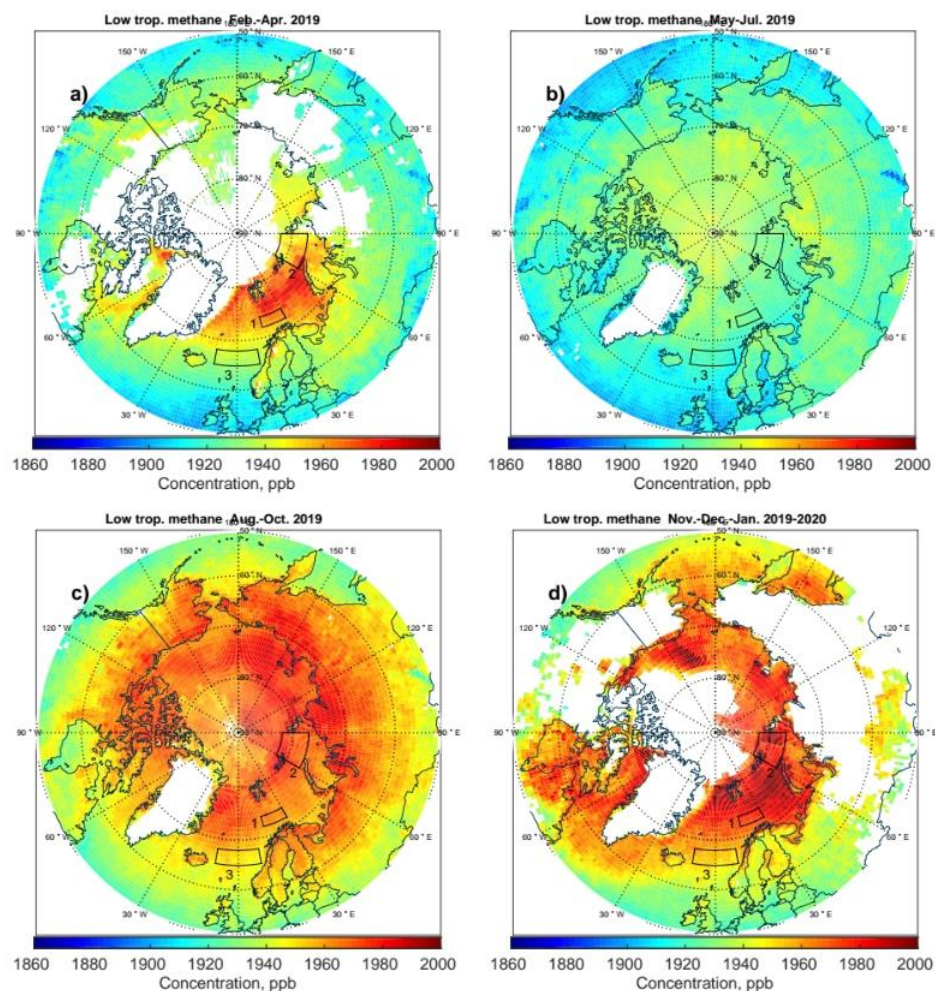203   in December–January and minimum in June–August.
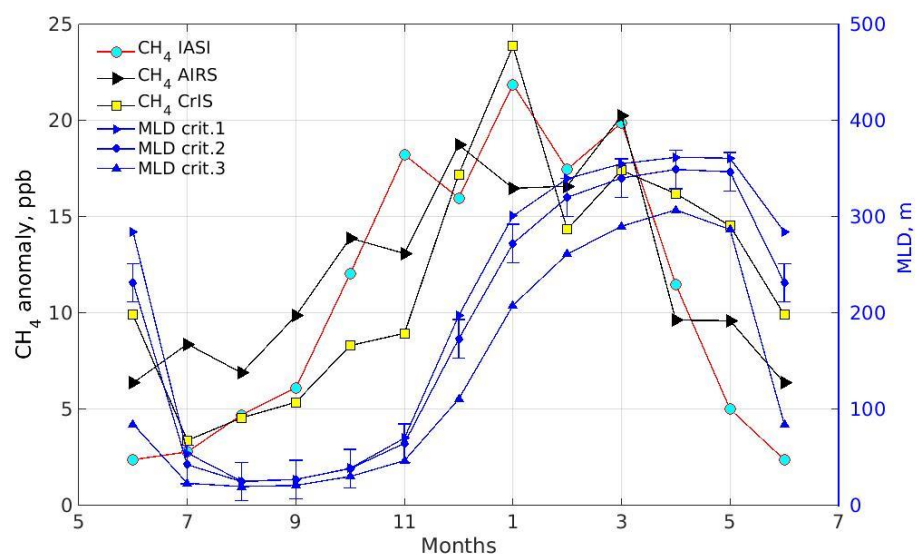
204   *Figure 1*

205   *Figure 2*

206   To explain this pattern, we computed MLD in domain #1 over the same time period using
207 three different criteria (see Methods). These MLD estimates have similar shapes, but somewhat

208 different magnitudes, which might be taken as an estimate of data accuracy. Kara et al. (2002)
209 estimated accuracy as ± 20 m for the data based on criterion #2. Only in June do the plots
210 diverge, otherwise disagreements do not exceed 50 m. Methane anomaly steeply grows in
211 October–November and reaches a maximum in January. MLD is very shallow in summer (~20-
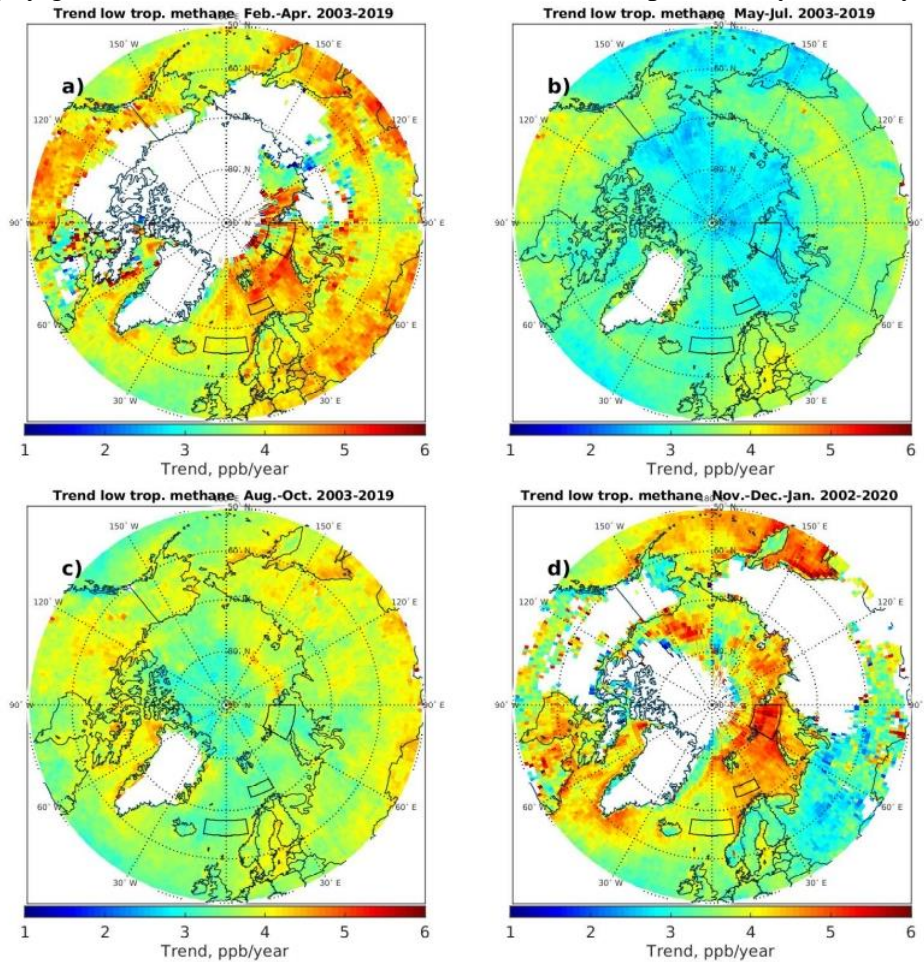212 30 m), abruptly grows between November and December, and plateaus by February.

213 *Figure 3*

214 A strengthening of winter anomalies throughout the seven-years-long period between
215 2010 and 2016 have been noted by Yurganov et al. (2017). A significantly longer period of the
216 AIRS data allows one to look into long-term changes in methane concentration and seasonal
217 amplitude. We computed a pan-Arctic maps of seasonally resolved methane trends during last
218 17 years (Figure 3 for LT and Figure S6 for MT). Linear least squares regressions were
219 calculated using MATLAB for each 1°x1° grid cell. This procedure allows us to locate regions
220 with the highest growth rates. The lowest trends, between 2.5 and 3.5 ppb/year were found in
221 summer over the mid-latitude Atlantic, Pacific, and some parts of the Arctic ocean including
222 domain #3 (Figure 3b). Continental summer trends over were slightly higher: up to 4 ppb/year.
223 The globally-averaged CH_4 trend for 2007–2014 was estimated from surface measurements as ~
224 5–6 ppb/year (Saunois et al., 2020), though it increased after 2014 (Yurganov et al., 2017; Nisbet
225 et al. 2019). A reduced sensitivity of the thermal IR remote technique to LT generally can lead to
226 underestimation of methane changes (0.3-0.5, see Methods and Yurganov et al., 2016). This
227 should be kept in mind while comparing LT satellite data with in situ surface measurements. On
228 the other hand, sensitivity of the TIR technique to MT is higher and close to one. This is a
229 reason for higher trends in MT (see Supplement Figure S6 and S7) . The maximal rate of long-

230   term winter LT methane growth up to 5.5 ppb/year was found to the north of the Kara Sea, as
231   well as over the northern Sea of Okhotsk (Figure 3d) that was twice as large compared to the
232   summer rate. From what was presented above, the central Barents Sea with the most strong
233   water mixing might be expected to demonstrate the fastest winter growing. However, it was not
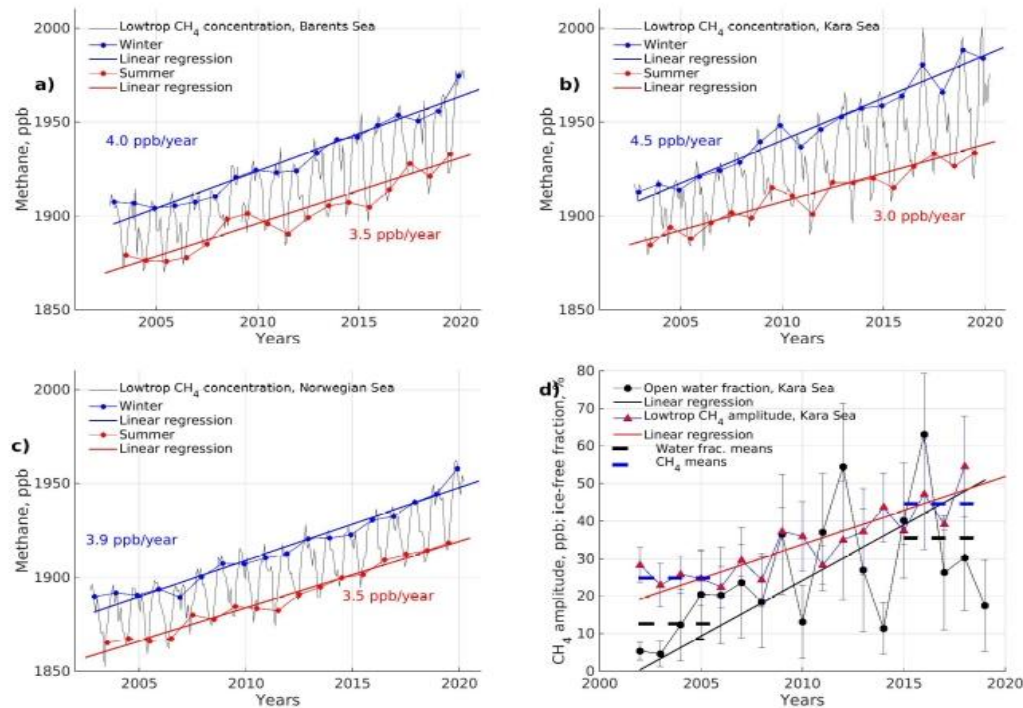234   the case: the largest winter trends were observed far to the North-East of that place, closer to the
235   domain #2.

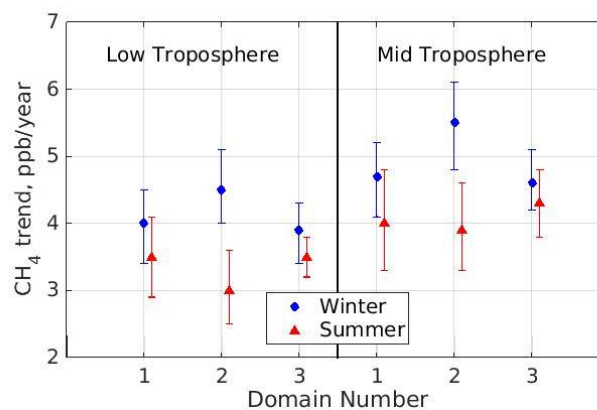236   *Figure 4*

237   *Figure 5*

238   Figure 4 a, b, c show monthly mean methane concentrations for domains ## 1, 2, 3,
239   respectively (thin black lines) and the amplitude trend for the domain #2 (winter minus summer,
240   red), Figure 4d. Parameters of linear least square correlation are listed in Table and on a graph of
241   Figure 5. For all domains winter trends are higher than summer trends, but the difference
242   between them is statistically significant for domain #2 only. One may compare this trend with
243   variations of the fraction of open water $C_{wat}=100-C_{ice}$, where C_{ice} is the fraction of ice in the
244   same domain. Open water fraction really increased from 2002 to 2019, but huge year-to-year

245   variations impede a search of correlation.

246   Growing seasonal methane amplitude over of the Kara Sea domain needs to be explained
247   at least in terms of secular changes in two transport mechanisms concerned in this paper. In spite
248   of direct correlation between methane and water fraction, it is reasonable to compare the maps of
249   open water and methane for the beginning and the end 5-year spans of data (spans are shown as
250   dashed lines in Figure 4d). In a map of Figure 6a, the winter open-water fraction averaged over
251   2014–2018 was subtracted by that over 2002–2006. The northern BKS region has the fastest ice
252   degradation in the Arctic Ocean (the indicated area between Svalbard, Severnaya Zemlya, and
253   Kara Sea is called the "big polygon" henceforth). The Arctic-wide record fast decline in sea-ice
254   in this area is a well known phenomenon that significantly disturbs the air circulation in Northern
255   mid and high latitudes (Petoukhov and Semenov, 2010; Zhang et al, 2018b). Similarly, ice
256   degradation during last 17 years may be a significant factor impacting the interannual variability
257   of methane (Figure 6b). Correlation between them is poor: maximal increase of open water area
258   is observed in the northernmost part of the big polygon, whereas CH_4 increased mostly close to
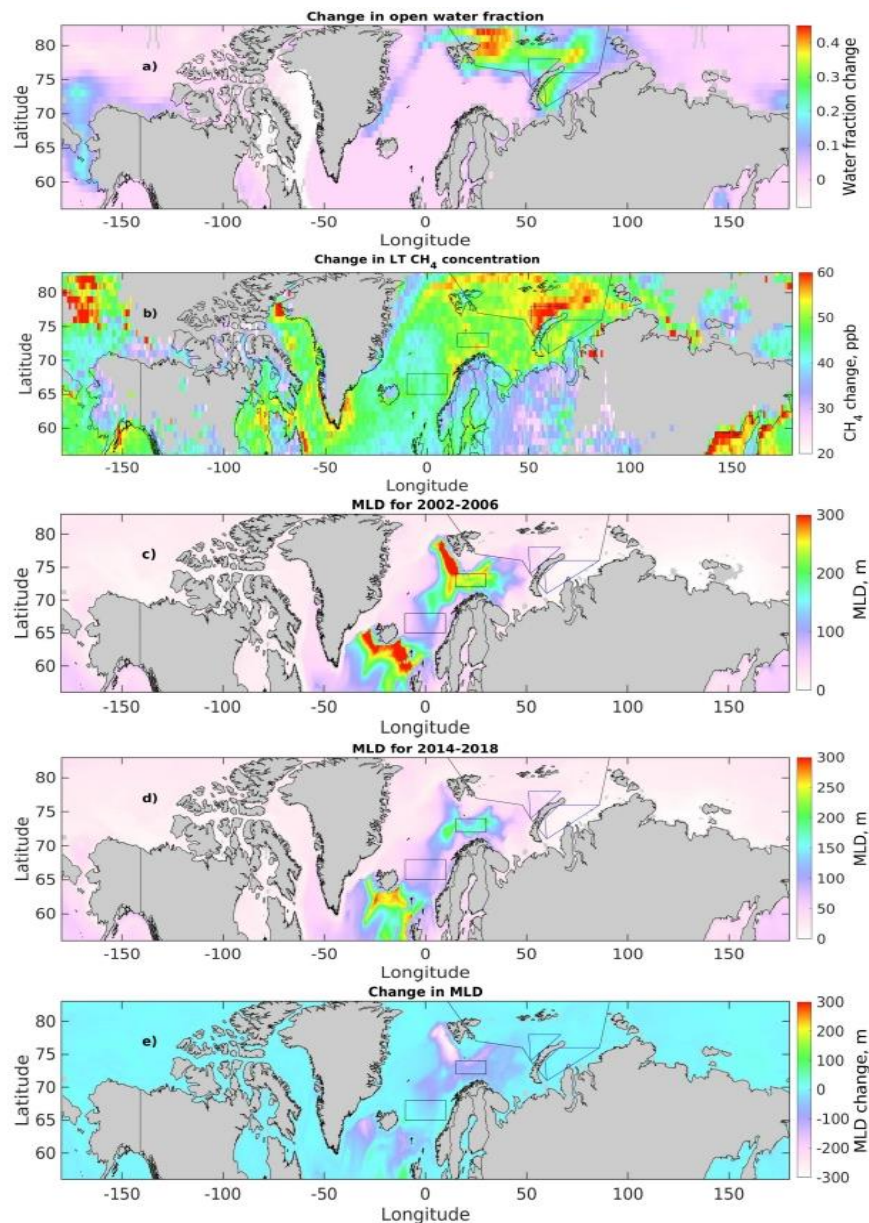259   NZ.

260   *Figure 6*

261   An illustration for that is Figure 7: methane for $1° \times 1°$ pixels from Figure 6b was plotted
262   versus corresponding pixels for open water fraction from Figure 6a. Methane for the big
263   polygon and the Kara Sea polygon dramatically increases with increasing water fraction from
264   0.08 to 0.15, but plateaus after. The number of points for the NZ polygon for low water (high
265   ice) conditions is insufficient to make any conclusions on connections with sea-ice cover decline
266   there. Data presented in Figure 7 show that there may be several mechanisms causing methane
267   increase in the big polygon since the beginning of this century, but growing area of open water is
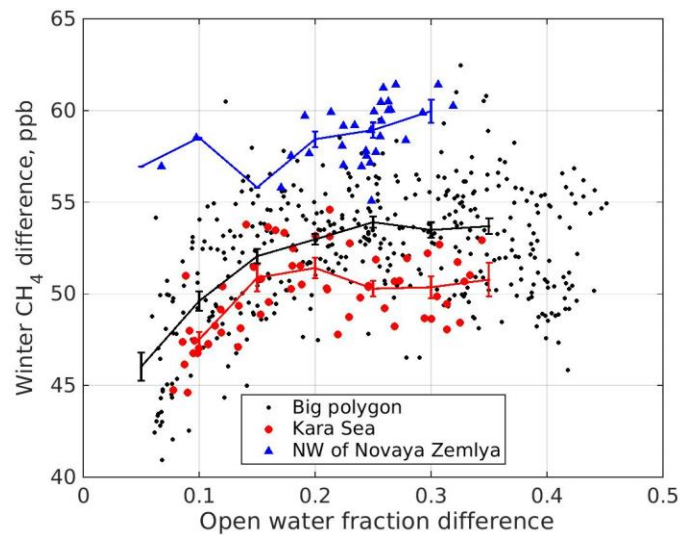268   one of them.

269   *Figure 7*

270   Long-term changes in MLD throughout the elapsed 17-year period may influence
271   methane in BKS. To check a feasibility of this, winter MLD were averaged for the Arctic over
272   the same 5-year spans and subtracted one from another (Figure 6 c,d, e). In contrast to C_{wat},
273   MLD diminished since the early 2000: changes were negative in the Barents Sea and west of
274   Svalbard. This decrease may be connected with secular changes in seawater stability. The
275   reasons for these require further analysis, but in fact this negative trend cannot be a reason for the
276   observed methane positive trend.

4. Discussion

278   Seven currently operative TIR spectrometers launched at sun-synchronous polar orbits
279   supply huge amounts of information about Arctic methane year-round, day and night. These TIR
280   data are unique for studying CH_4 emissions from a warming Arctic, both terrestrial and marine.
281   Results presented in this paper evidence in favor of wintertime Arctic seas as an important source
282   area for the regional methane budget. In spite of a reduced sensitivity, preference has been made
283   to methane in low troposphere. This atmospheric layer is supposed to be more closely linked
284   with surface emissions. MT AIRS retrievals are more sensitive to CH_4 variations in this layer, but
285   in the 4-6 km altitudes the long-range transfer of trace gases is very important. Nevertheless,
286   MT data show patterns that similar to LT (Supplement Figures S6 - S8). Further investigation
287   should be based on 3D modeling using actual wind fields.

288   Global methane emission is estimated by Saunois et al. (2020) as 576 Tg CH_4 per year.
289   High latitude (60° N - 90° N) emission constitutes only 23 Tg CH_4 per year, i.e., ~4%. Marine
290   emission is considered by Saunois et al. (2020) and Berchet et al. (2016) as negligible (<4 Tg
291   CH_4 per year). Satellite data (Yurganov et al., 2016) are in agreement with low sea/air flux in
292   summer, but in cold season the Arctic seas appear to contribute ~ 2/3 of annual continental
293   emission (i.e., ~15 Tg CH_4 per year). In any case, even 38 Tg CH_4 per year is less than 7% of
294   global budget. Growing amplitude of the CH_4 seasonal cycle, observed by AIRS over the Arctic
295   shelf since 2003, evidence a growing winter flux. Nevertheless, the Arctic contribution hardly
296   can be expected to surpass 10% of global emission even in the near future. Influence of growing
297   CH_4 Arctic emission for the global trend should not be large. Contrary to that a regional
298   influence may be significant. These speculations need a further investigation.

299   A thorough discussion of methane sources in the Arctic is beyond the scope of this study.

300 Our goal is just to indicate points of interest for further investigation. This study focuses at
301 natural barriers for sea/ice exchange in BKS: summertime stable stratification and wintertime sea
302 ice cover. In summer the pycnocline retains dissolved methane in deep layers and makes it
303 available for methanotrophic bacteria. Atmospheric CH_4 concentration grows after November
304 (Figure 2) concurrently with disappearance of the pycnocline and MLD deepening; its bottom
305 boundary reaches a level of ~150 m. Available summer direct sounding data (Mau et al., 2017,
306 Supplement Figure S9) indicate this depth as an upper boundary of high dissolved methane
307 concentrations.   Enhanced mixing facilitates gas transport to the surface and winter becomes a
308 season of maximal methane flux to the atmosphere.

309   Second barrier is mostly important for seas that partially ice covered. Northern BKS ice
310 cover has a distinct trend of degradation since the beginning of this century, especially in early
311 winter (Figure 6a). Sea ice is a natural barrier for the flux and methane emission grows with
312 years. Inter-relations between the flux and ice decay in winter may be more complicated. One
313 can not exclude that the radiative forcing of excess methane may be a significant component in
314 the warming of this area and, prospectively, for the whole Arctic. In other words, a positive feed-
315 back is possible and investigation of methane emission from the Arctic seas must be intensified.

316 5. Conclusions

317   Data of three TIR orbital instruments for the Arctic seas allow to detect enhanced
318 methane over BKS in winter. This finding highlights significant roles of turbulent diffusion in
319 seawater depth and ice cover for the sea/air methane exchange. Enhanced mixing in winter
320 resulted in a maximum of excess methane during that season in the western Barents Sea. 17-
321 years long period of AIRS monitoring reveals an area with growing seasonal amplitude of both
322 LT and MT methane: between Svalbard, Franz Josef Land, Novaya Zemlya and Severnaya
323 Zemplya archipelagos. This is interpreted in terms of growing methane flux due to decay of ice
324 cover: the area is known for record fast ice degradation. A trend in methane flux from the seabed
325 itself was not considered here due to lacking experimental data.

326 Acknowledgments

339

340 References

341 Årthun, M., Eldevik T. , and Smedsrud L. H. (2019), The role of Atlantic heat transport in future
342   Arctic   winter   sea   ice   loss.   *Journal   of   Climate,   32*,   3327–3341,
343   https://doi.org/10.1175/JCLI-D-18-0750.1.

344 Berchet A., Bousquet P., Pison I., et al. (2016), Atmospheric constraints on the methane
345   emissions from the East Siberian Shelf, *Atmospheric Chemistry and Physics*, *16*: 4147–

346   4157, https://doi.org/10.5194/acp-16-4147-2016.

347   Bloom H. J. (2001), The cross-track infrared sounder (CrIS): a sensor for operational
348   meteorological remote sensing, in Fourier Transform Spectroscopy, *OSA Trends in Optics*
349   *and   Photonics*,   *3*,   1341–1343,   Optical   Society   of   America   ,   doi:
350   10.1109/IGARSS.2001.976838.

351   de Boyer Montégut D. Madec, G., Fischer, A. S., Lazar, A., and Iudicone, D.   (2004), Mixed
352   layer depth over the global ocean: An examination of profile data and a profile-based
353   climatology,   *Journal   of   Geophysical   Research*,   *109*,   C12003,
354   doi:10.1029/2004JC002378.

355   Cavalieri D. J., Parkinson C. L., Gloersen P., Zwally H. J. (1996), Sea Ice Concentrations from
356   Nimbus-7 SMMR and DMSP SSM/I-SSMIS Passive Microwave Data, Version 1.
357   Boulder, Colorado USA. NASA National Snow and Ice Data Center Distributed Active
358   Archive Center, doi: https://doi.org/10.5067/8GQ8LZQVL0VL.

359   Comiso J. C., Parkinson C. L., Gersten R., Stock L(2008), Accelerated decline in the Arctic sea
360   ice cover. *Geophysical Research Letters*,. *35*, L01703. doi: 10.1029/2007GL031972,

361   Fekete B. M., Vöröosmarty C. J., and Grabs W. (2002), High-resolution fields of global runoff
362   combining   observed   river   discharge   and   simulated   water   balances.   *Global*
363   *Biogeochemical Cycles*, *16*(3), 1042.

364   Fenty I.,   Menemenlis D., and   Zhang H. (2017), Global Coupled Sea Ice-Ocean State
365   Estimation. *Climate Dynamics*, *49*(3), 931–956.

366   Ferré B., Jansson P., Moser M., Serov P., Portnov A.D., Graves C. , Panieri G., Gründger F.,
367   Berndt C., Lehmann M.F., Niemann H. (2020), Reduced methane seepage from Arctic
368   sediments during cold bottom-water conditions. *Nature Geoscience, 13*, 144–148.
369   https://doi.org/10.1038/s41561-019-0515-3

370   Forget, G., Campin, J.-M., Heimbach, P., Hill, C. N., Ponte, R. M., and Wunsch, C. (2015),
371   ECCO version 4: an integrated framework for non-linear inverse modeling and global
372   ocean state estimation. *Geoscientific Model Development*, *8*(10), 3071–3104.

373   Gambacorta, A. (2013), The NOAA unique CrIS/ATMS processing system (NUCAPS):
374   algorithm   theoretical   basis   documentation,   available   at:
375   hhttp://www.ospo.noaa.gov/Products/atmosphere/soundings/nucaps/docs/NUCAPS_ATB
376   D_20130821.pdf

377   Gent, P. and McWilliams J. (1990), Isopycnal mixing in ocean circulation models, *Journal of*
378   *Physical Oceanography*, *20*, 150–155.

379   Gentz T., Damm E., von Deimling J. S., Mau S.,McGinnis D. F., Schlüter M. (2014), A water
380   column study of methane around gas flares located at the West Spitsbergen continental
381   margin. *Continental Shelf Research*, *72*, 107- 118 . doi: 10.1016/j.csr.2013.07.013

382   Hoegh-Guldberg O. and Bruno J. F. (2010), The impact of climate change on the world's marine
383   ecosystems. *Science*, *328*, 1523-1528. doi: 10.1126/science.1189930

384   James R. H., Bousquet P., Bussmann I., Haeckel M., Kipfer R., Leifer I., Niemann H., Ostrovsky
385   I., Piskozub J., Rehder G., Treude T., Vielstadte L., Greinert J. (2016) Effects of climate
386   change on methane emissions from seafloor sediments in the arctic ocean: a review.
387   *Limnology and Oceanography*, *61*, S283–S299. https://doi.org/10.1002/lno.10307

388   Kara, A. B., Rochford, P. A., & Hurlburt, H. E. (2000), An optimal definition for ocean mixed

389 layer depth. *Journal of Geophysical Research, 105*(C7)*, 16803–16821.
390   doi:10.1029/2000JC900072.

391 Kara A. B., Rochford P. A., Hurlburt H. E. (2002), Mixed layer depth variability over the global
392   Ocean. *Journal of Geophysical Research*, *108*(C3), doi: 10.1029/2000JC000736

393 Maddy E. S., Barnet C. D., Gambacorta A. (2009),   A computationally efficient retrieval
394   algorithm for hyperspectral sounders incorporating a priori information. *IEEE
395   Geoscience Remote Sensing Letters*, *6,* 802–806, doi:10.1109/lgrs.2009.2025780.

396 Mau S., Romer M., Torres M.E., Bussmann I., Pape T., Damm E., Geprags P., Wintersteller P.,
397   Hsu C.W., Loher M., Bohrman G. (2017), Widespread Methane Seepage along the
398   Continental Margin off Svalbard—From Bjornoya to Kongsfjorden. *Scientific Reports*, *7*,
399   42997 https://doi.org/10.1038/srep42997

400 Menemenlis, D., Fukumori, I., & Lee, T. (2005a), Using Greens functions to calibrate an ocean
401   general circulation model, *Monthly Weather Review, 133*, 1224–1240.

402 Menemenlis, D., Hill, C., Adcroft, A., Campin, J., Cheng, B., Ciotti, B., et al. (2005b). NASA
403   supercomputer improves prospects for ocean climate research. *Eos Transactions AGU
404   86(9)*, 95–96. doi: 10.1029/2005EO090002

405 Menemenlis, D., Campin, J., Heimbach, P., Hill, C., Lee, T., Nguyen, A., Schodlock, M., &
406   Zhang, H. (2008), ECCO2: high resolution global ocean and sea ice data synthesis,
407   *Mercator Ocean Quarterly Newsletter*, *31*, 13–21.

408 Myhre C.L., Ferré B., Platt S.M., Silyakova A., Hermansen O., Allen G., et al. (2016), Extensive
409   release of methane from Arctic seabed west of Svalbard during summer 2014 does not
410   influence the atmosphere, *Geophysical Research Letters, 43*, 4624–4631.

411   Myhre, G; Shindell, D.; Bréon, F.M.; Collins, W.; Fuglestvedt, J.; Huang, J.; Koch, D.;
412   Lamarque, J.F.; Lee, D.; Mendoza, B.; Nakajima, T.; Robock, A.; Stephens, G.;
413   Takemura, T.; Zhang, H. (2013), *Climate Change 2013: The Physical Science Basis.
414   Contribution of Working Group I to the Fifth Assessment Report of the Intergovernmental
415   Panel on Climate Change* , T. F. Stocker, D. Qin, G.-K. Plattner, M. Tignor, S.K. Allen, J.
416   Boschung, A. Nauels, Y. Xia, V. Bex and P.M. Midgley, Cambridge University Press,
417   Cambridge, United Kingdom and New York, NY, USA, 2013

418 Nisbet, EG; Manning, MR; Dlugokencky, EJ; Fisher, RE; Lowry, D; Michel, SE; Lund Myhre,
419   C; Platt, SM; Allen, G; Bousquet, P; Brownlow, R; Cain, M; France, JL; Hermansen, O;
420   Hossaini, R; Jones, Anna ; Levin, I; Manning, AC; Myhre, G; Pyle, JA; Vaughn, B;
421   Warwick, NJ; White, JWC. (2019), Very strong atmospheric methane growth in the four
422   years 2014 - 2017: Implications for the Paris Agreement. *Global Biogeochemical Cycles*,
423   *33*(3). 318-342. https://doi.org/10.1029/2018GB006009

424 Olivier, J.G.J., Van Aardenne, J.A., Dentener, F., Pagliari, V., Ganzeveld, L.N., & Peters, J.A.
425   (2005), Recent trends in global greenhouse gas emissions: regional trends 1970-2000 and
426   spatial distribution of key sources in 2000. *Environmental Sciences, 2* (2-3), 81-99. doi:
427   10.1080/15693430500400345.

428 Petoukhov V., Semenov V. A. (2010), A link between reduced Barents Kara sea ice and cold
429   winter extremes over northern continents. *Journal of Geophysical Research, 115*,
430   D21111. doi:10.1029/2009JD013568.

431 Portnov A., Mienert J., Serov P. (2014), Modeling the evolution of climate sensitive Arctic
432   subsea permafrost in regions of extensive gas expulsion at the West Yamal shelf. *Journal

433   *of   Geophysical   Research*:   *Biogeosciences*,   *119*(11):   2082-94.
434   https://doi.org/10.1002/2014JG002685

435   Razavi A., Clerbaux C., Wespes C., Clarisse L., Hurtmans D., Payan S., Camy-Peyret C., &
436   Coheur P. (2009), Characterization of methane retrievals from the IASI space-borne
437   sounder. *Atmospheric Chemistry and Physics, 9*, 7889-7899.

438   Redi, M. H. (1982), Oceanic isopycnal mixing by coordinate rotation. *Journal of Physical
439   Oceanography*, *12*, 1154–1158.

440   Rudels, B. (1993), High latitude ocean convection. In Flow and Creep in the Solar System:
441   Observations, Modelling and Theory, pp. 323–356. Ed. by D. B. Stone and S. K.
442   Runcorn. Academic Publishers, Dordrecht.

443   Saunois M. et al. (2020), The global methane budget 2000–2020. *Earth System Scientific Data,
444   12*, 1561–1623, https://doi.org/10.5194/essd-12-1561-2020.

445   Serov, P., Vadakkepuliyambatta, S., Mienert, J., Patton, H., Portnov, A., Silyakova, A., et al.
446   (2017), Postglacial response of Arctic Ocean gas hydrates to climatic amelioration.
447   *Proceedings   of   the   National   Academy   of   Sciences , 114*(24),   6215–6220.
448   doi:10.1073/pnas.1619288114

449   Shipilov E. V., Murzin R. R. (2002), Hydrocarbon deposits of western part of Russian shelf of
450   Arctic—Geology and systematic variations. *Petroleum Geology*, *36*(4): 325–347.
451   [Translated from Geologiya Nefti i Gaza. 2001, no. 4, 6–19.]

452   Skagseth, Ø., Eldevik, T., Årthun, M. et al. Reduced efficiency of the Barents Sea cooling
453   machine. *Nature Climatic Change*, *10*, 661–666 (2020). https://doi.org/10.1038/s41558

454   Smith, N., and Barnet C. D. (2019), Uncertainty characterization and propagation in the
455   Community Long-term Infrared Microwave Combined Atmospheric Product System
456   (CLIMCAPS). *Remote Sensing*, *11*, 1227, https://doi.org/10.3390/rs11101227.

457   Suga, T., K. Motoki, Y. Aoki, and A. M. Macdonald (2004), The North Pacific climatology of
458   winter mixed layer and mode waters. *Journal of Physical Oceanography*, *34*, 3–22.

459   Susskind, J., Blaisdell J. M., and Iredell L. (2014), Improved methodology for surface and
460   atmospheric soundings, error estimates, and quality control procedures: The Atmospheric
461   Infrared Sounder science team version-6 retrieval algorithm. *Journal of Applied Remote
462   Sensing*, *8*(1), 084994, https://doi.org/10.1117/1.JRS.8.084994.

463   Sweeney, C., Dlugokencky, E., Miller, C. E., Wofsy, S., Karion, A., Dinardo, et al. (2016), No
464   significant increase in long-term CH_4 emissions on North Slope of Alaska despite
465   significant increase in air temperature. *Geophysical Research Letters, 43*, 6604–6611,
466   doi:10.1002/2016GL069292

467   Wunsch, C., Heimbach, P. Ponte, R., and Fukumori, I. (2009), The global general circulation of
468   the ocean estimated by the ECCO-consortium. *Oceanography, 22*, 88-103.

469   Xiong X, Barnet C, Maddy E, Sweeney C., Liu X., Zhou L., Goldberg M. (2008),
470   Characterization and validation of methane products from the Atmospheric Infrared
471   Sounder (AIRS). *Journal of Geophysical Research* , *113***, G00A01,
472   doi:10.1029/2007JG000500.

473   Xiong X., Barnet C., Maddy E., Gambacorta A., King T., and Wofsy S. (2013), Mid-upper
474   tropospheric methane retrieval from IASI and its validation, *Atmospheric Measurement
475   Techniques, 6*, 2255-2265.

476   Yurganov L. N., Leifer I., Myhre C. L. (2016), Seasonal and interannual variability of
477   atmospheric methane over Arctic Ocean from satellite data. *Sovremennye problemy*
478   *distantsionnogo zondirovaniya zemli iz kosmosa (Current Problems of Remote Sensing of*
479   *Earth From Space), 13*(2): 107-119, doi:10.21046/2070-7401-2016-13-2-107-119

480   Yurganov L.N., Leifer I., and Vadakkepuliyambatta, S. (2017), Evidences of accelerating the
481   increase in the concentration of methane in the atmosphere after 2014: satellite data for
482   the Arctic), *Sovremennye problemy distantsionnogo zondirovaniya zemli iz kosmosa*
483   *(Current Problems of Remote Sensing of Earth From Space), 14(5)*, 248-258. doi:
484   10.13140/RG.2.2.16613.29927

485   Yurganov L., Muller-Karger F., Leifer I. (2019), Methane increase over the Barents and Kara
486   Seas after the autumn pycnocline breakdown: Satellite observations. *Advances in Polar*
487   *Science*, *30*(4):382-390. doi: 10.13679/j.advps.2019.0024

488   Zhang, H., Menemenlis, D., and Fenty, I. G. (2018a), ECCO LLC270 Ocean-Ice State Estimate,
489   https://doi.org/1721.1/119821

490   Zhang Q., Xiao C., Ding M., Dou T. (2018b), Reconstruction of autumn sea ice extent changes
491   since AD1289 in the Barents-Kara Sea, Arctic. *Science China Earth Science*, *61,* 1279–
492   1291. https://doi.org/10.1007/s11430-017-9196-4

493

494 **Figure captions.**

495　Figure 1. Methane concentrations retrieved from AIRS TIR radiance data for the layer 0-4 km
496　(LT) for 4 seasons: spring (a), summer (b), autumn (c), winter (d) between February, 2019 an
497　January, 2020. Blank areas correspond to insufficient vertical air temperature contrast (ThC<10°
498　C). See also the same for MT (Supplement, Figure S5).

499　Figure 2. LT (0-4 km altitude) CH_4 anomaly, i.e. a concentration difference between the Barents
500　Sea domain #1 and Norwegian Sea domain #3 (see map Figure 1). IASI and AIRS data are
501　averaged over 2010-2018, CrIS data are for 2015-2018. Blue lines are 2010-2018 averaged
502　MLD for the Western Barents Sea domain #1 (see map) for 3 criteria (#1 is by Suga et al.
503　(2004), #2 is Kara et al. (2000) , #3 is Boyer et al. (2004).

504　Figure 3. Maps of LT methane trends derived from 2002-2019 data of AIRS. Slopes of standard
505　linear regression lines for 4 seasons: spring (a), summer (b), autumn (c), winter (d)   were
506　computed for each 1°x1° lat/lon pixel. Blank areas correspond to insufficient vertical air
507　temperature contrast (ThC<10° C) . See also the same for MT (Supplement, Figure S6).

508　Figure 4. Methane LT concentrations and trends according to AIRS data. Monthly mean methane
509　concentrations are averaged for domains, designated on the maps of Figure 1: a) #1, b) #2, and c)
510　#3. Regression lines are plotted for winter and summer periods, slopes are shown (see also Table
511　and Figure 5). d): Amplitudes of seasonal cycles for Kara Sea domain #2 are computed as
512　difference between CH_4 for winter period and for the next summer period. They are compared
513　with mean fractions of open water for the same domain in winter (November-January). Dash
514　lines are CH_4 and C_{wat} averaged for the first and last 5-year spans. See also the same for MT (
515　Supplement, Figure S7).

516　Figure 5. Slopes of regression lines for two seasons, three domains, and two altitude ranges.
517　Error bars correspond to Lower and Upper bounds of confidence intervals for slope (reliability
518　95%). See also Table.

519　Figure 6. Maps of open water fraction, CH_4 and MLD (criterion #2). a) Changes in winter open
520　water fraction   averaged over the first 2002-2006 and last 2014-2018 spans of AIRS
521　measurement period. b) The same, but for LT CH_4 concentration. c) MLD   for 2002-2006. c)
522　MLD for 2014-2018. e) Map d) subtracted by map c).

523　Figure 7. Spacial correlation between changes in open water fraction (Fig. 6a) and LT methane
524　concentrations (Fig. 6b) for big polygon and two sub-polygons (indicated on the maps of Figures
525　6a and 6b). Each point corresponds to 1°x1° pixel. Lines connect averages for binned CH_4, error
526　bars are STD $\cdot$ N$^{-1/2}$, where STD are standard deviations for binned data, N is number of points.
527

528 **Table**

529 *Linear Regression Parameters For CH$_4$ Seasonal Means in ppb/year. LBCI Is Lower Bound of*
530 *Confidence Interval for Slope; UBCI is Upper Bound of Confidence Interval for Slope (reliability*
531 *95%). See also Figure S8. R is correlation coefficient*

Domain	Layer	Season	Slope	LBCI	UBCI	R
1	LT	Winter	4.0	3.4	4.5	0.94
2	LT	Winter	4.5	4.0	5.1	0.95
3	LT	Winter	3.9	3.4	4.3	0.95
1	MT	Winter	4.7	4.1	5.2	0.94
2	MT	Winter	5.5	4.8	6.1	0.95
3	MT	Winter	4.6	4.2	5.1	0.96
1	LT	Summer	3.5	2.9	4.1	0.90
2	LT	Summer	3.0	2.5	3.6	0.89
3	LT	Summer	3.5	3.2	3.8	0.97
1	MT	Summer	4.0	3.3	4.8	0.88
2	MT	Summer	3.9	3.3	4.6	0.90
3	MT	Summer	4.3	3.8	4.8	0.96
1	LT	Win.-Summ.	1.3	0.7	1.9	0.34
2	LT	Win.-Summ.	2.2	1.4	3.0	0.55
3	LT	Win.-Summ.	0.9	0.5	1.3	0.25
1	MT	Win.-Summ.	1.6	0.9	2.3	0.38
2	MT	Win.-Summ.	2.5	1.5	3.4	0.52
3	MT	Win.-Summ.	1.0	0.6	1.5	0.28

532

533

534

535

536

537

538